



Electron beam welding of 2205 duplex stainless steel with nickel-based filler wire using multi-beam technique

Tamás Tóth¹ · Jonas Hensel² · Ann-Christin Hesse¹ · Klaus Dilger¹

Received: 19 March 2022 / Accepted: 4 August 2022 / Published online: 29 August 2022
© The Author(s) 2022

Abstract

The duplex stainless steels have many favorable properties attributed to their two-phase microstructure consisting of almost equal fractions of ferrite and austenite. Therefore, they are widely used in the offshore, petroleum, and chemical industries as a base material for pressure vessels and pipelines. Such components often possess large thicknesses, which can be effectively welded with electron beam. This process is characterized by rapid cooling combined with a relatively great loss of nitrogen, resulting in insufficient austenite formation. To compensate this phenomenon, the addition of nickel, in the form of wire, was performed in this study. This promoted the formation of austenite at the same cooling rate, so that approximately an equal amount of ferrite and austenite was achieved. Beam oscillation was applied to maintain good dilution even at large depth/width ratios. Furthermore, the multi-beam technique was implemented to reduce the spatter formation and provide a higher process stability. This allows the spatial, but not temporal, separation of the melting-off of the wire and the main welding process. The joints produced in this way exhibit a good weld dilution and consequently an austenite distribution with a low inhomogeneity. Additionally, a narrow heat-affected zone was produced.

Keywords Electron beam welding · Duplex stainless steel · Nickel · Microstructure · Austenite · Ferrite · Beam oscillation · Weld dilution

Nomenclature

EB	Electron beam
EBW	Electron beam welding
LBW	Laser beam welding
LMD	Laser metal deposition
TIG	Tungsten inert gas
wt. %	Percentage by weight
DSS	Duplex stainless steels

BM	Base metal
HAZ	Heat-affected zone
FZ	Fusion zone
OES	Optical emission spectroscopy
EDS	Energy-dispersive spectroscope
SCC	Stress corrosion cracking
SEM	Scanning electron microscopy
U	Accelerating voltage
v_w	Welding speed
v_F	Wire feed speed
D	Focal distance
I_b	Beam current
Q	Line energy
SW_x	Oscillation length
SW_y	Oscillation width
F	Oscillation frequency
F_{Switch}	Jumping or switching frequency of the beam
DC_x	Offset in the x-direction
DC_y	Offset in the y-direction
f	Defocusing
P	Percentage of the total power in the respective zone of the weld pool
ISO	International Organization for Standardization

✉ Tamás Tóth
t.toth@tu-braunschweig.de

Jonas Hensel
jonas.hensel@mb.tu-chemnitz.de

Ann-Christin Hesse
a.hesse@tu-braunschweig.de

Klaus Dilger
k.dilger@tu-braunschweig.de

¹ Institute of Joining and Welding, Technische Universität Braunschweig, Langer Kamp 8, 38106 Braunschweig, Germany

² Chair of Welding Engineering, Chemnitz University of Technology, Reichenhainer Straße 70, 09126 Chemnitz, Germany

EN European Standard
 NORSOK Norsk Søkkel Konkurransesjjon (in Norwegian)—Norwegian Continental Shelf Competition Position

1 Introduction

1.1 General

The duplex stainless steels (DSS) are defined as alloys with a two-phase structure, in which both phases, ferrite and austenite, are present with a fraction of 30–70 %, based on the Fe-Cr-Ni-N alloy system [1, 2]. Considering the corrosion and the mechanical properties, the optimum phase balance is in the range of 45% and 60%. Due to the balanced microstructure, the DSS generally possess higher tensile strength, a better pitting corrosion resistance, and lower susceptibility to chloride stress corrosion cracking (SCC) than austenitic stainless steels. This main advantage leads to an ever-increasing use of DSS in various products, most of which are exposed not only to high mechanical loads but also to diverse corrosive environments. The DSS solidify as ferrite and remain ferritic until the end of the solidification; the austenite transformation starts approximately around 1200 °C, depending on the actual chemical composition. The extent of ferrite-austenite transformation, and thus the amount of precipitated austenite, is determined by two factors: the time spent at elevated temperatures, primarily between 1200 and 800 °C, and the chemical composition of the underlying alloy. In terms of the latter, a distinction is made between elements that stabilize either the ferrite or the austenite. Chromium, molybdenum, silicon, niobium, and titanium stabilize the ferritic phase. In contrast, carbon, nickel, manganese, nitrogen, and copper promote the formation of the austenitic phase [3]. The DSS gain their phase balance and the consequent beneficial mechanical properties through precise adjustment of the chemical composition, combined with controlled cooling.

1.2 Power beam welding of duplex stainless steels

The DSS are commonly used in thick-walled components such as pressure vessels, pipelines, autoclaves, or desalination units, which are primarily made of sheet metals cold- or hot-formed and subsequently welded. Beam welding processes such as laser beam welding (LBW) or electron beam welding (EBW) offer several technical and economic advantages. They offer the possibility of an automated, one-sided welding sequence creating a single-pass bead without the need to turn the components to weld a back bead [4]. This beneficial characteristic made EB-welded DSS components particularly attractive for the oil and gas industry, e.g., for

longitudinally welded tubular products. Problems associated with multi-layer seams [5], such as process delays due to interpass cooling or cleaning, uncontrolled distortions or undesired microstructural changes resulted from a layer-wise build-up can also be avoided to a great extent. One significant challenge when using power beam processes is the rapid cooling of the weld zone, not providing enough time for the austenite formation [6]. This results in a very high ferrite fraction and leads to nitride precipitation not only in the heat-affected zone (HAZ) but also in the fusion zone (FZ) due to the limited nitrogen solubility of the ferrite [7, 8]. In order to understand the phase transformations and the various precipitations in the weld zone, the heat-affected zone and the fusion zone should be discussed separately. The reason for this is that the HAZ and the FZ are subjected to different physical-chemical mechanisms, which should be considered when discussing the microstructure.

1.3 Behavior of the heat-affected zone of duplex stainless steels in power beam welding

In the HAZ, the chemical composition remains unaltered. The influence of diffusion-driven processes on the chemical composition on macroscopic scale can be considered negligible at the cooling speeds commonly used for welding processes. These mechanisms rather involve element migration or segregation on microscopic or even atomic scale (e.g., element segregation to grain boundaries [9]). The HAZ can be further divided into three distinct zones: partially melted zone, delta ferrite grain growth zone, and partially transformed zone. Partial melting takes place in the immediate proximity to the fusion line. This region is characterized to be within a two-phase field, which is a mixture of ferrite (δ) and liquid [10]. Moving towards the base metal, the delta ferrite grain growth zone follows. In this zone, the temperature rises above the δ solvus line. In this temperature range, the single phase δ ferrite is thermodynamically stable and the microstructural changes are governed by the $\delta + \gamma \rightarrow \delta$ transformation. The degree of ferritization and consequently the amount of dissolved austenite depends on the thermal history experienced above the δ solvus line, the initial phase ratio, and the chemical composition of the alloy. Higher nitrogen contents impede the ferritization and, as a result, reducing the geometrical extension of this zone, as reported by Corolleur et al [11]. Subsequent to the dissolution of the austenite (γ), rapid growth of the ferrite grains occurs. During the cooling, the ferrite partially decomposes into austenite ($\delta \rightarrow \gamma + \delta$). The cooling speed, and hence the time spent between roughly 1200 and 800 °C ($t_{12,8}$), determines the extent to which this reformation takes place, thus determining the final phase ratio. The furthest zone related to the weld metal (partially transformed zone) still experiences temperatures, although for only a short time, which

are sufficient to partially dissolve the austenite with limited ferrite grain growth. Depending on the initial microstructure of the base material, small changes can take place in the phase balance, but generally the microstructure of this zone is not significantly altered. Even though the development of a HAZ, particularly the delta ferrite growth zone, cannot be evaded, its phase ratio can be clearly influenced. Varbai et al. [12] reported about the phase evolution in HAZs of 2205 DSS. With increasing cooling time, the austenite fraction rises due to the prolonged time available for the austenite reformation. Above a cooling time ($t_{12,8}$) of 10 s, austenite contents above 40% can be achieved. Using tungsten inert gas (TIG) welding with a heat input of 2.0 kJ/mm, the HAZ exhibits a maximal width of 200 μm . Yang et al. [13] also revealed a strong correlation between the cooling time and the amount of reformed austenite.

1.4 Effect of nitrogen effusion and thermal cycle on the microstructure of the fusion zone

In the FZ, different mechanisms govern. The beneficial effects of the prolonged cooling are suppressed by nitrogen effusion from the fusion zone and hence cannot be exploited when the shielding gas does not contain any nitrogen fraction. The negative effects of the nitrogen loss on the austenite formation even outweigh the positive effects of the prolonged cooling time at higher heat input [14]. This frequently occurs in laser beam welding but also in arc welding processes when solely argon protects the weld pool [12, 14, 15]. In electron beam welding, the partial pressure of the nitrogen is obviously practically zero as a high-vacuum is utilized [16–18]. Since nitrogen is a very strong austenite stabilizer, its loss impedes the formation of austenite during cooling. Adding nitrogen to the shielding gas results in an enlarged austenite fraction in the weld metal, as proven by several authors [19–23]. However, this is not an option in EBW due to process limitations. When nitrogen is not applied, two basic opportunities remain to improve the phase balance. The first one covers an intervention on the part of the thermal cycle, decelerating the cooling between 1200 and 800 °C. This can be mostly done by utilizing a pre-heating or a post-welding heat treatment directly integrated into the welding process. Fey et al. [24] have successfully presented an approach in LBW, which is based on a two-beam method. The first focused laser beam completes the welding. The second beam creates a diffuse temperature field as it is formed through a diffractive optical element. This realizes a post-heating, which promotes the formation of spherical intragranular austenite. Krasnorutskiy et al. [25] investigated a multi-beam EBW process to realize an in situ pre-heating. Their approach consists of a multi-beam technology for welding the thick-walled components of DSS without the need for a filler material or a post-weld heat treatment.

Having several spots in a row along the welding direction, the forerunning spots create a pre-heating for the upcoming ones. Thus, the last spot welds in a significantly preheated material, leading to a promoted austenite formation. However, if more than 4 spots are used, the nitrogen loss induced by the multiple remelting outweighs the pre-heating effect, leading to a drop in the austenite fraction. Given that no filler metal is added, a post-welding heat treatment adequately increases the austenite fraction, solving also the nitrides and the intermetallic phases precipitated before. However, this process step not only costs time but also requires a high amount of technical capital.

1.5 Effect of nickel addition on the microstructure of the fusion zone

Adding nickel to the weld pool, which is an austenite stabilizer, a post-welding heat treatment may be used to fulfill the requirements of standards. This approach has become the subject of several studies as the balanced microstructure generally entails prospering mechanical properties [26]. Wu et al. [27] performed laser beam welding tests on 2205 DSS with nickel powder addition. Coaxial powder feed at a flow rate of a few grams per minute led to the increase in the austenite fraction. Strasse et al. [28] conducted laser beam welding on duplex plates, whose edges were previously clad by means of laser metal deposition (LMD), using nickel-based powder. The enrichment of the surface with nickel led to a balanced austenite/ferrite ratio and thus improved corrosion resistance. A more obvious form of the nickel is a wrought product, which has the benefit of being commercially more available in the form of nickel-based wires used mostly in high-temperature applications. Additionally, standardized wire diameters offer the possibility to realize the material feed via wire feed. Although pre-placed filler wires may be also an option [8], an automated wire feeder unit can be easily integrated into a LBW or EBW machine and does not require any edge preparation such as a groove for the pre-placing. One challenge to be solved is the fine distribution of the nickel wire along the weld depth; otherwise, only the upper regions will be enriched with nickel. Due to the flexibility of the EBW, beam oscillation can be applied to modify the weld geometry, the weld pool dynamics and to improve the dilution between the filler wire and the base metal [29]. The so-called multi-beam or multi-process technique allows the free configuration of multiple weld pools, weld pools with complex energy distribution or even temperature fields. Although no beam splitting takes place, the electron beam alternates between the weld pools rapidly so that the process stability, even in keyhole mode, can be maintained [30]. The underlying study deals with the implementation of the multi-beam technique in welding of DSS with nickel-based filler wire. A further goal is to

characterize the joints in terms of their metallurgical, microstructural and mechanical properties.

2 Materials and methods

2.1 Materials

The base material used for the experiments was a 1.4462 standard duplex steel plate (Outokumpu 2205) with a thickness of 15 mm. To achieve over-alloying and consequently a higher austenite fraction of the weld metal, a 2.4607 (S Ni 6059 or NiCr23Mo16 according to EN ISO 18274) nickel-based filler wire (Böhler Thermanit Nimo C24) with a diameter of 1 mm was applied. The nominal chemical compositions of these wires determined by optical emission spectroscopy (OES) are shown in Table 1.

The plates had a length of 300 mm and a width of 150 mm, resulting in a total specimen size of 300 mm × 300 after welding.

2.2 Electron beam welding

The welding of the DSS plates was carried out by using a high-vacuum EBW machine (K26-3 by pro-beam, Gilching, Germany) with a maximal output power of 15 kW. The used welding machine and the welding layout are depicted in Fig. 1. The wire feeding was performed by using a built-in wire feeder unit.

Altogether two test plates (one without and another one with weld pool backing) were welded with slightly different values for beam current (I_b) and wire feed speed (v_F), due to the fact that the welding without weld pool backing requires a lower energy input and consequently results in a smaller cross-sectional area of the joint. The accelerating voltage (U), the welding speed (v_w), and the working distance (D) were kept constant during the entire experimental procedure. The contact tube and consequently the wire, had a trailing angle of 30°. To produce a weld with weld pool backing, a higher beam current was required, which led to a larger joint cross-section. To provide a nearly equal nickel content in the FZ, the wire feed speed was adjusted accordingly. The basic process parameters of the electron beam welding are given in Table 2.

Table 1 Nominal composition of the base material and the filler wire

Chemical composition (wt. %)											
Material	C	Cr	Ni	Mn	Si	Mo	Nb	N	Fe	Cr _{Eq} *	Ni _{Eq} *
BM: 1.4462	0.026	22.8	5.48	1.29	0.34	3.07	0.001	0.183	Bal.	27.5	9.3
FW: 2.4607	0.013	22.9	60.1	0.17	0.07	15.8	0.056	-	Bal.	-	-

Table 2 The applied basic process parameters in the electron beam welding

Test Nr.	Weld pool backing	U (kV)	v_w (mm/s)	v_F (m/min)	D (mm)	I_b (mA)	Q (kJ/mm)
1	No	120	6	2.3	871	71	1.42
2	Yes	120	6	2.7	871	80	1.60

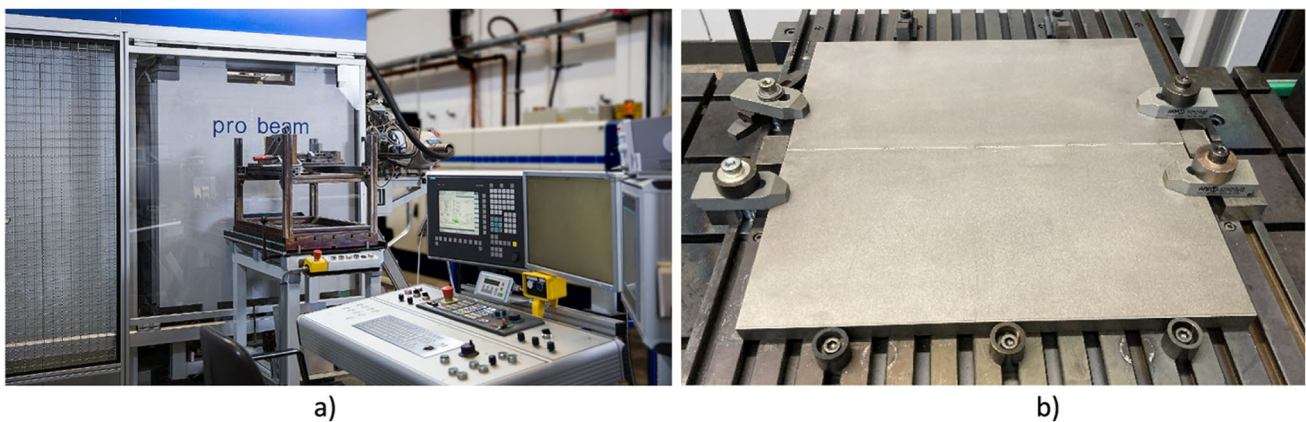


Fig. 1 The electron beam welding machine (a) and the clamping setup of the specimens (b)

During the EBW, the multi-beam technique was applied to provide a controlled, spatial but not temporal decoupling between the melting of the wire and the main welding sequence. The beam deflection was configured to create two distinct zones in the weld pool without weld pool separation. In the first zone (1), the melting of the wire occurs with an undeflected but defocused (f) beam. The second zone (2) created a wide weld seam which, due to the large oscillation width, also allows a sufficient mixing between the base metal and the filler wire. Here, a deflection pattern having a shape of an “infinity” is applied (see Fig. 2), which was previously developed and investigated in previous experiments [31]. The pattern possess a length of 5 mm (SW_x), a width of 3.8 mm (SW_y), and oscillates with a frequency (F) of 150 Hz. Its central point was moved 2.5 mm backward (DC_x) in the x -direction related to the undeflected beam axis having the coordinate of (0,0). To provide a good process stability, the beam switches back and forth between the two zones 10 000 times per second, whereby a (relatively high) frequency of 10 kHz (F_{Switch}) is given. It should be noted, that the beam does not spend the same amount of time in each zone. Considering the total welding duration as 100 %, the beam spends 10 % being defocused at the (0,0) point and 90 % oscillating according to the pattern. Therefore, a theoretical power ratio (P) of 1:9 between the zone 1 and zone 2 is given, not considering that the beam leaves a tiny fraction of the total energy input between the zones as it is not switched off while alternating with a finite velocity. The focal point was also alternating its position by using the built-in dynamic lens. In zone 1, it was 60 mm above the plate surface to increase the process stability during the melting, while zone 2 used a

defocusing of +22.5 mm. An overview of the multi-beam parameters is shown in Table 3.

2.3 Metallographic and metallurgical investigations

The main focus of this study lays on the microstructure obtained through using the nickel-based filler wire in the diverse regions of the fusion zone (FZ). Subsequent to the welding, the plates were cut into pieces using a water jet cutter. The specimens dedicated for the metallographic investigations were first ground and polished, then etched with Beraha-II reagent (70 ml distilled water + 30 ml HCl + 0.5 g $K_2S_2O_5$), coloring the different phases. Altogether two metallographic specimens were extracted from each plate: one 30 mm from the beginning of the weld seam (pos. A) and another 30 mm from the end (pos. B) in order to gain information about the process stability (see Figure 5). The metallographic investigation of the joints involved the examination of the weld geometry and the detailed evaluation of the FZ and the HAZ. Considering a large depth/width ratio and a limited time available for a complete dilution, an inhomogeneous distribution of the nickel and consequently that of the ferrite fraction may be of concern. Hence, five images were captured from the top, middle, and bottom region of the FZ, respectively. A DM4000M incident light microscope (Leica, Wetzlar, Germany) was utilized for this step. To calculate a ferrite fraction, several possibilities exist. Determining the ferrite number (FN) is associated with challenges as the EB weld seam is much narrower compared to arc welded joints, and thus, the influence of the base material is significant. It is therefore evident that a point-counting method [32], or an automated image analysis [33] of the captured images

Fig. 2 Schematic illustration of the beam oscillation parameters

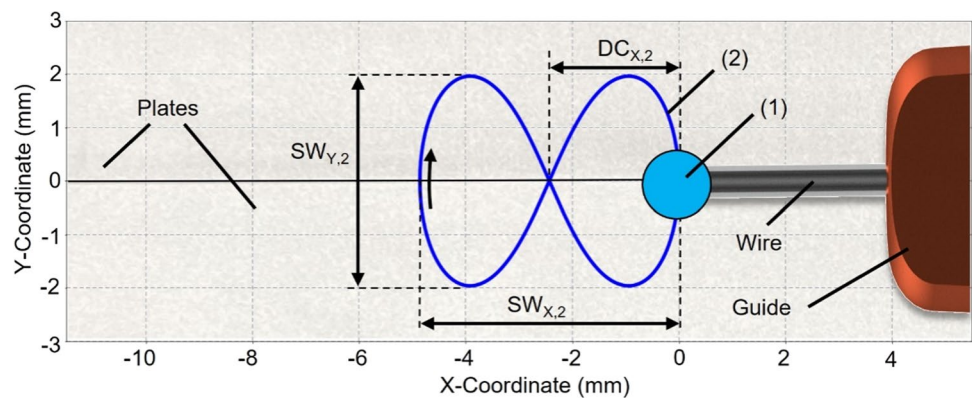


Table 3 The applied parameters of the multi-beam technique in the electron beam welding

Zone	Pattern	SW_x (mm)	SW_y (mm)	DC_x (mm)	DC_y (mm)	f (mm)	P (%)	F (Hz)	F_{Switch} (kHz)
1	Defocused spot	0	0	0	0	+60.0	10	-	10
2	“Infinity”	5	3.8	-2.5	0	+22.5	90	500	

provide the most reliable results in the underlying case. To exclude human factors and to allow a reproducible process, an automated image analysis according to ASTM E1245 [33] with a magnification of 500 \times and a custom-made script was applied. To distinguish between austenite and ferrite, several possibilities exist. Common of all is that they require a good sample preparation and a sufficient contrast between the austenite and ferrite phases to allow a clear distinction mostly based on the “gray scale” image values. The images were loaded in 8-bit, giving a range of possible “gray scale” image values from 0 to 255 for each pixel. By analyzing the histogram, the second issue is the threshold level that clearly determines the acquired ferrite fraction by counting a respective pixel either as austenite or ferrite. The phase ratio is simply the ratio between the number of dark pixels and the total number of pixels. Some studies recommend to set the threshold value to the arithmetic mean of the indices (grey values) of the ferrite peak and the austenite peak. This works well for samples where the microstructure contains more ferrite than austenite. In this case, this calculating method slightly overestimates the amount of ferrite, providing a more conservative calculation. However, the same applies if more austenite has been formed. Based on previous experiences, this method entails a risk if the amount of austenite significantly exceeds that of the ferrite. Especially at the upper normative limit (65% or 70% austenite, depending on the standards), overestimating the ferrite fraction is not desirable, nor is it safe in terms of component integrity. Hence, a modification was performed. It has been found in manual experiences that choosing the index belonging to the dip (considering the histogram trend) between the two peaks as a threshold leads to a more accurate result. In order to image this trend and exclude the noise, a Savitzky-Golay filter (window length: 15, polynomial order: 3) was applied to the histogram for the purpose of smoothing the data. This type of filter does not distort the course and keeps

the location of maxima and minima of the data curve. This is essential to maintain the locations of the peaks. From this filtered dataset, the lowest value was chosen as the threshold as presented in Fig. 3a. Once the threshold is known, a modified binarization took place. The threshold possesses a band (± 30 grey value) around itself, where the pixels are neither considered to be ferrite nor austenite, since they represent the grain boundaries (analogous to [32]), as presented in Fig. 3 (b-3₂). Pixels with gray values below this range are considered as ferrite and colored blue in the image. Obviously, gray values above this range represent the austenitic phase and colored yellow (see Fig. 3 (b-3₁)). Subsequent to the calculation of the respective pixels, the phase balance and the scale are also written on the analyzed image, as shown in Fig. 3 (b-4).

For revealing the sigma-phase and the possible chromium nitride precipitations, a further electrochemical etching was performed. These were performed first by using an aqueous solution of 20% NaOH then a 10% oxalic acid (6 V for 10 s in both cases), respectively. The specimens were repolished between these two steps to remove the oxide layer formed during the etching.

The metallographic investigations may reveal information about the distribution of the ferrite but do not provide unambiguous information about the distribution of the nickel. The cooling rate, which may not be constant throughout the fusion zone, also plays a crucial role. Therefore, the distribution of the nickel was measured along the penetration depth by means of energy-dispersive spectroscopy (EDS). A JSM-6480 (JEOL, Freising, Germany) scanning electron microscope equipped with an eumeX detector was used for this examination. The machine was operated with an accelerating voltage of 20 kV. During the measurements, rectangular fields of 500 $\mu\text{m} \times 500 \mu\text{m}$ were scanned along the centerline from the top region to the root with a distance of 1 mm between the individual scan fields.

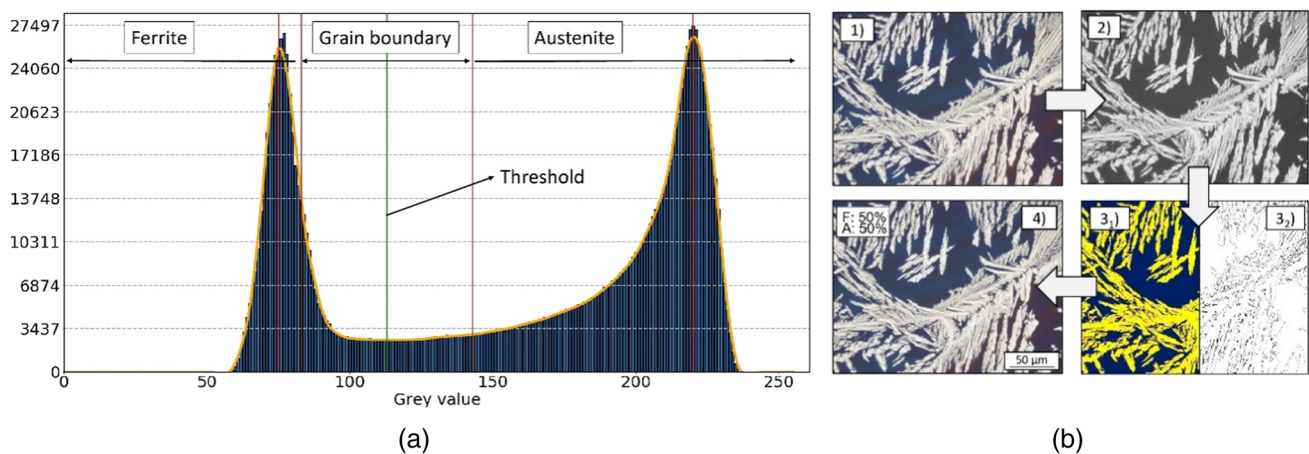


Fig. 3 The histogram analysis (a) and the sequences of the automated image analysis (b)

Additionally, the nitrogen content of the weld metal was determined by using carrier gas hot extraction (CGHE). With focus on the nitrogen loss in the different regions of the weld metal, test pieces having a width of 2 mm, a height of 4 mm, and a length of 10 mm (total weight per specimen: approximately 0.6 g) were extracted from the upper and the lower regions, as illustrated in Figure 4.

2.4 Investigation of the mechanical properties

Besides the metallographic investigations, hardness testing (HV1) was performed on the same cross-sections. Altogether 30 indents were placed normal to the centerline in each region of the joint (top, middle, and bottom). In the top and the bottom regions, the measurements took place

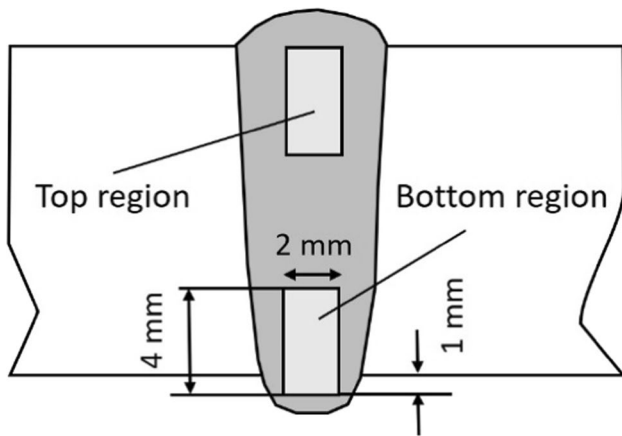


Fig. 4 The specimen extraction locations for the measurement of the nitrogen loss

1.5 mm below the surface. The distance between the individual indents was 0.25 mm. Furthermore, the determination of the absorbed impact energy values was also the subject of the study, as the impact toughness is of crucial importance when discussing DSS weldments. Altogether six Charpy-V notch specimens were extracted from the center of the plate. The first 3 specimens originated from the bottom region of the FZ, the remainder from the top region, respecting the welding direction. The Charpy-V impact tests were carried out at $-46\text{ }^{\circ}\text{C}$ (requirement of the NORSOK M-601 [34] and the NORSOK M-630 [35]) conforming to the EN ISO 148-1 [36] and evaluated according to the EN ISO 17781 [37]. Finally, tensile tests were performed at room temperature, using a strain rate of 0.00025 s^{-1} . Having a reduced section length of 64 mm, this results in a crosshead speed of 0.96 mm/min. The specimens had a thickness of 5 mm and a width of 16 mm on the reduced section. The schematic illustration of the specimen extraction is depicted in Fig. 5.

3 Results

3.1 Microstructure

Figures 6 and 7 show the weld geometry of the test 1 highlighted after color etching. Attributed to the “infinity”-shaped oscillation pattern, the fusion lines are parallel to each other. This weld shape promotes the dilution between the filler wire and the base material compared to a V-shaped geometry where no significant dilution in the lower regions would be expectable. Two minor disadvantages are the cold lapping on the top and the excessive root penetration, which should be either remelted or removed by machining. Taking

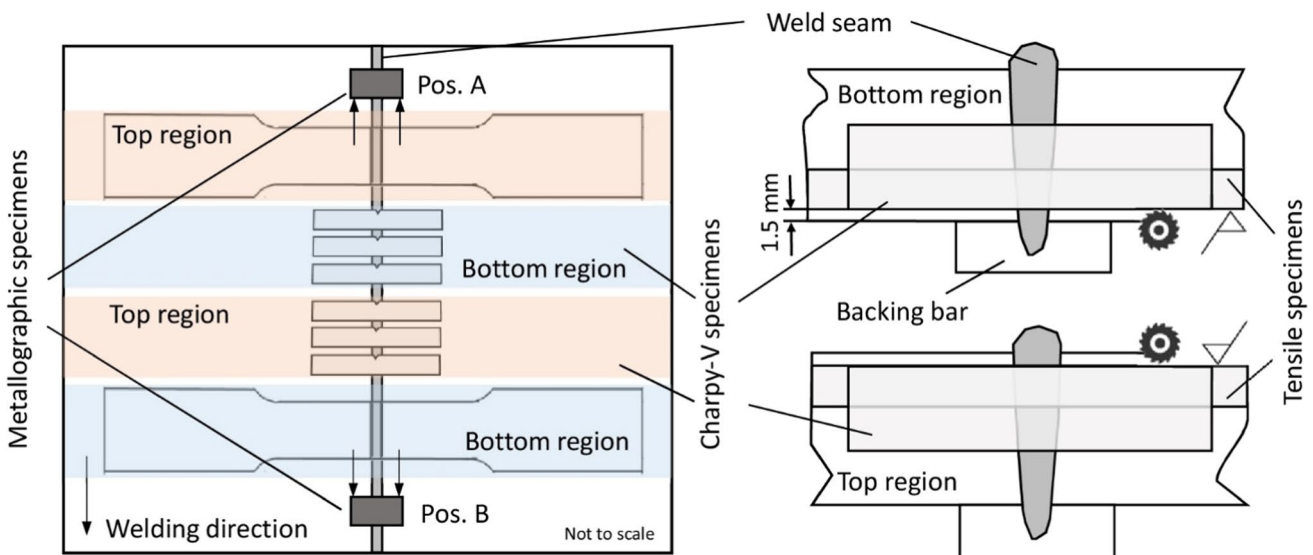


Fig. 5 The extraction of the metallographic cross-sections and the Charpy-V specimens using the example of the test 2

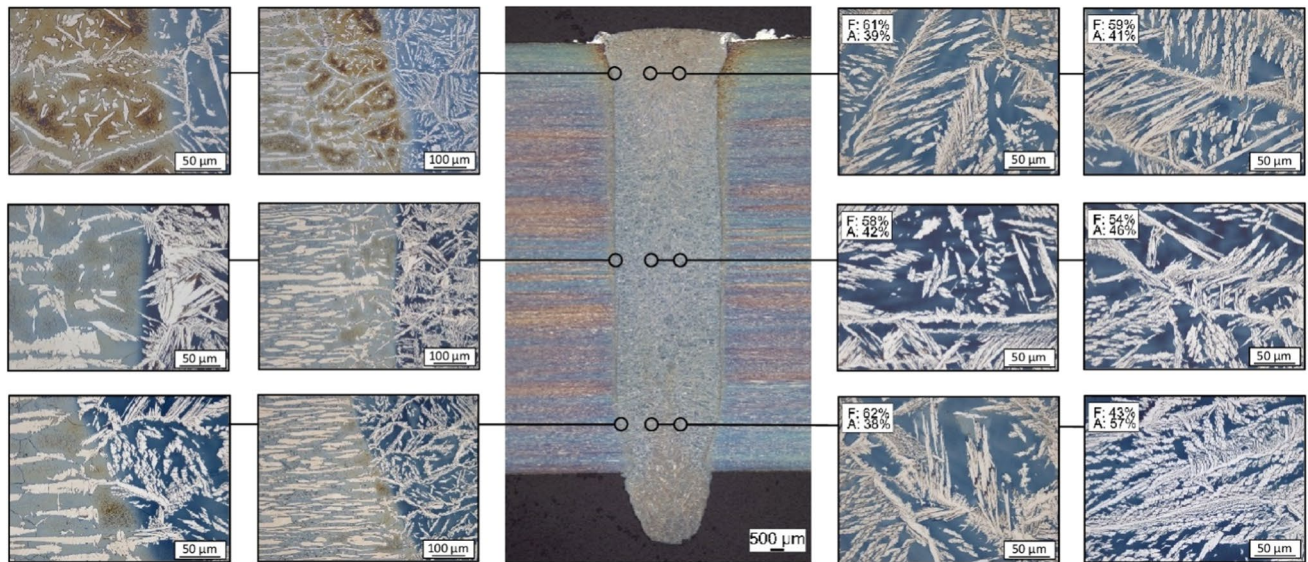


Fig. 6 Weld geometry and the microstructure of the test 1 (beginning of the seam: pos. A), highlighting the HAZ and the FZ

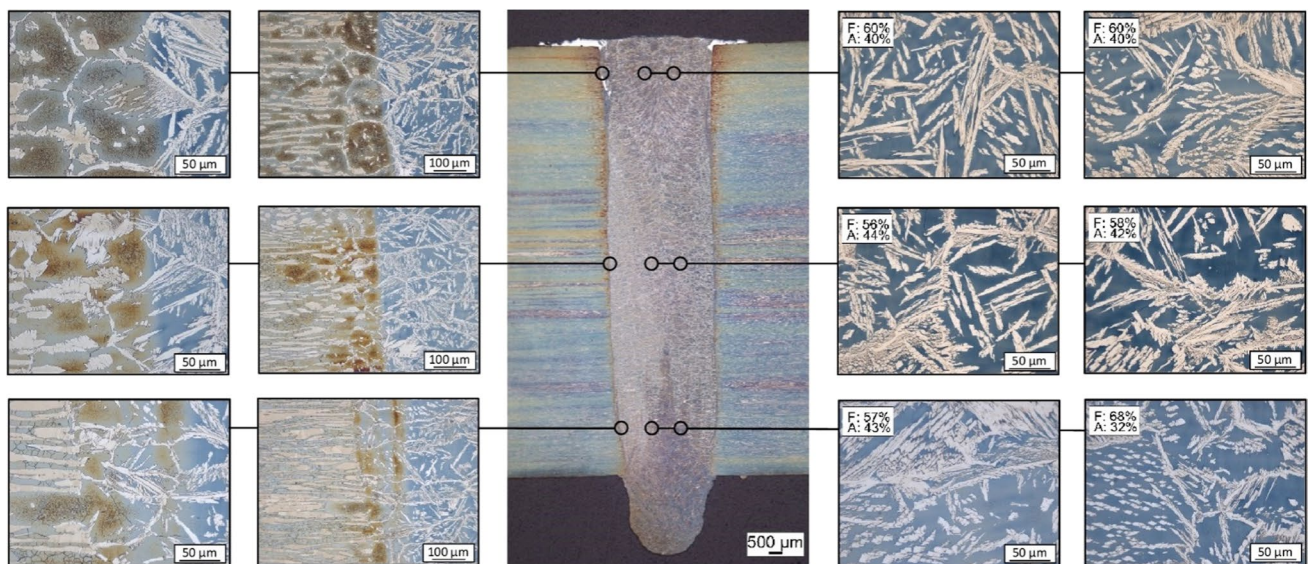


Fig. 7 Weld geometry and the microstructure of the test 1 (end of the seam: pos. B), highlighting the HAZ and the FZ

the force of gravity into consideration, this excessive drop-out cannot be avoided due the flat welding position and the comparably high amount of molten metal. When analyzing the microstructure, a balanced austenite-ferrite ratio can be observed. Higher ferrite fractions amounting to 60–65% can be found solely in the root drop-out, especially at the pos. B. Considering that it is commonly removed during a subsequent process step, it is not of critical importance. The top and middle regions of the FZ contain 50–60% ferrite and therefore fulfill the formulated criteria of various standards and technical recommendations [34, 35, 37, 38].

These regions are characterized by the presence of Widmanstätten austenite and allotriomorphic austenite, while intragranular austenite usually appears only in the bottom regions. Although the FZ can be effectively modified by the nickel-based filler wire, it is not the case in the HAZ. Its microstructure is primarily determined by its thermal history experienced during the heating and the subsequent cooling, and by its initial chemical composition, neglecting any diffusion processes. The HAZ has a pronounced width of 200–250 μm on the top side, since the energy coupling also occurs from this direction. Here, large ferrite grains can be

observed, which are surrounded by allotriomorphic austenite on their boundaries, containing secondary austenite inside.

Figures 8 and 9 show the weld geometry of the test 2, which was produced with weld pool backing. Compared to the weldment without weld pool backing, an excessive cap height can be observed on the top side. On both sides of the weld cap, cold lapping occurs, which may have detrimental effect on crevice corrosion if it is not removed afterward. Nevertheless, removing through machining or remelting with TIG is a common industrial practice. It should be noted that a subsequent remelting may lead to either a higher or a

lower ferrite fraction. This depends on whether the stabilizing effect of the nickel combined with a slower cooling overweighs the impeding effect which occurs due to the nitrogen loss. This balance is determined by the actual chemical composition and the cooling rate. The microstructure contains, similar to the test 1, a high amount of austenite, creating a balanced phase ratio even in the lower regions. In the HAZ, similar observations can be formulated as in the case of the test 1. The HAZ has a pronounced width of 200–250 μm in the top region, while it is only partially recognizable in the lower regions.

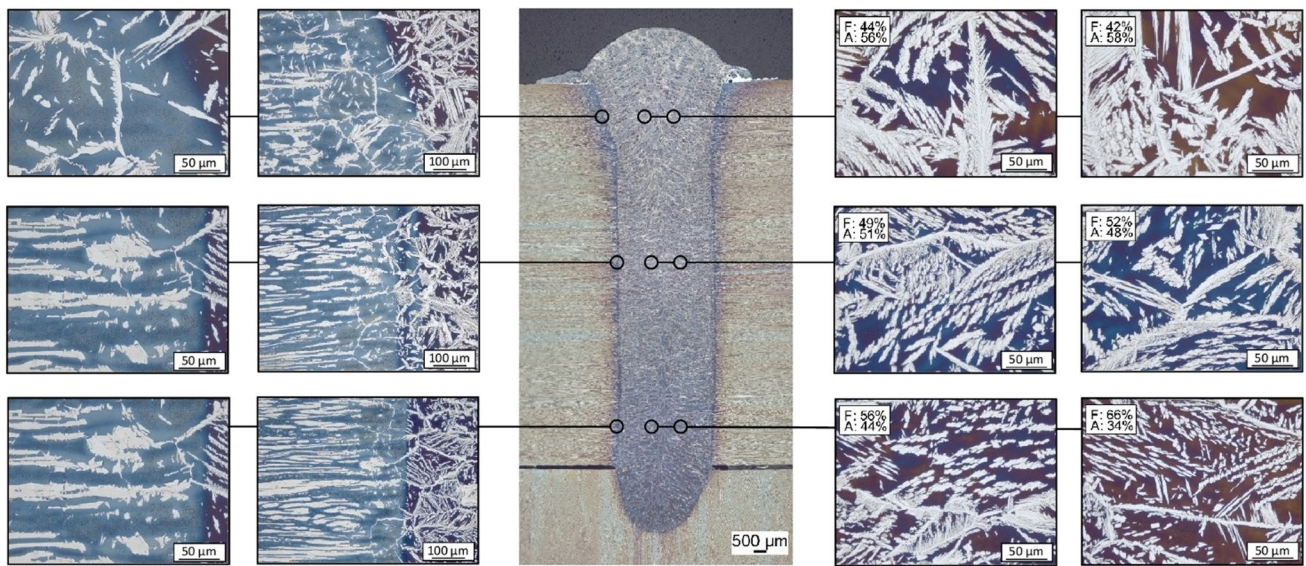


Fig. 8 Weld geometry and the microstructure of the test 2 (beginning of the seam: pos. A), highlighting the HAZ and the FZ

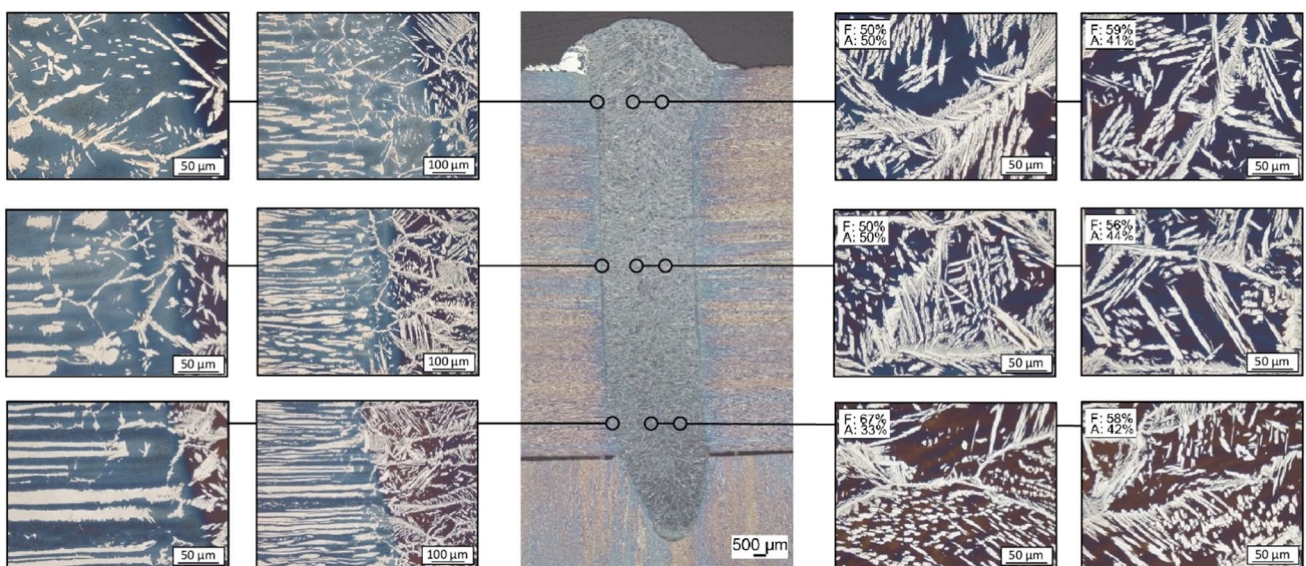


Fig. 9 Weld geometry and the microstructure of the test 2 (end of the seam: pos. B), highlighting the HAZ and the FZ

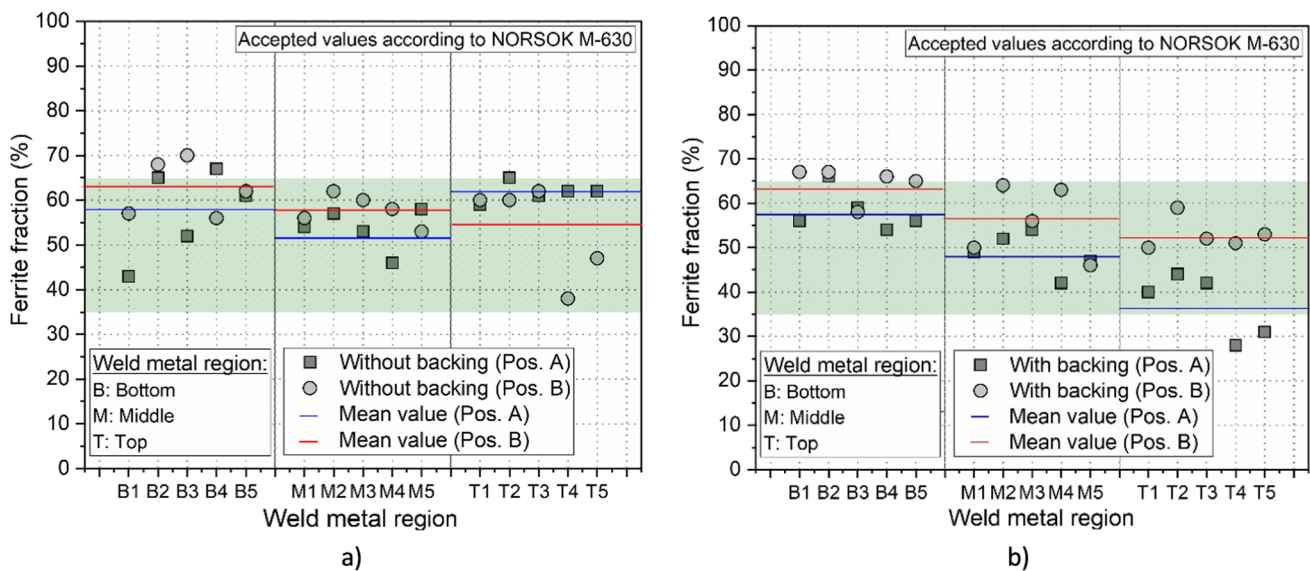


Fig. 10 The ferrite fractions in the different regions of the weld metal (**a** test 1; **b** test 2)

Figure 10 gives an overview of the acquired ferrite fraction values in the different regions of the weld metal. By analyzing the results obtained in the test 1, no clear decreasing trend can be observed. The mean ferrite fraction values are in the range of 50–65%, fulfilling the requirements formulated by the Norsok M-601 [34] and Norsok M-630 [35]. The test 2, to the contrary, shows a different tendency, especially when the pos. A is under discussion. There, a clear decreasing trend in the ferrite fraction values is outlined. Especially the upper region possesses lower ferrite fraction values, although the mean value still remains in the range of acceptance.

When welding DSS, not only the phase balance but also the presence of different intermetallic phases is important.

Figure 11 highlights the images captured after etching with 20% NaOH. Unmixed filler wire could be observed along the fusion line in the top region of the joint (see the numbered regions of interest (ROI) with a dashed border). On their boundaries, regions colored dark brown can be noticed, especially around ROI “1.” These inclusions are naturally rich in nickel and molybdenum; thus, the presence of intermetallic phases (e.g., sigma phase) cannot be excluded. Nevertheless, such indications for possible precipitation can be solely seen around these inclusions. There is no evidence of sigma-phase neither in the FZ nor in the HAZ.

A further focus lies on the formation of chromium nitrides, which commonly occur when the microstructure is mostly ferritic. Since the nitrogen solubility of the

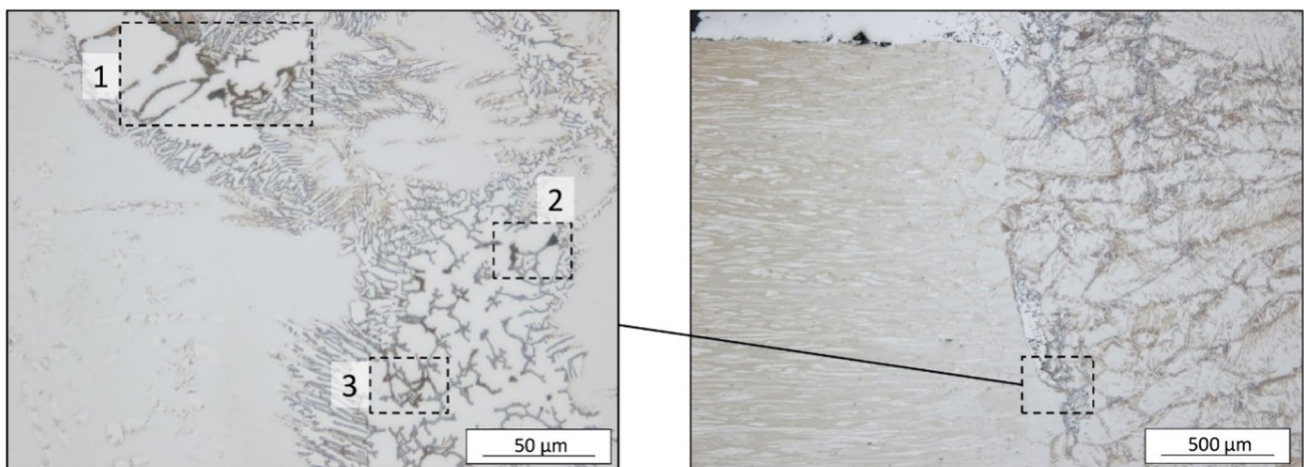


Fig. 11 Inclusions of the filler wire along the fusion zone revealed after electrochemical etching with NaOH (test 1; pos. B)

ferritic phase is much lower than that of the austenite, the chromium nitrides precipitate in the ferrite grains and occasionally along the grain boundaries [39]. Figure 12 illustrates the microstructure of the test 2 after etching with 10% oxalic acid. The FZ, and of course the BM, is free from any nitride precipitations. In contrast, the HAZ, especially in the upper region, consists of large ferrite grains. Inside them, chromium nitride precipitations was detected. These manifest themselves as clusters of finely dispersed nitrides as shown in ROI “4” and “5.”

3.2 Nickel distribution along the weld centerline

Figure 13 presents the distribution of the nickel content along the weld depth when welding without weld pool backing. Basically, a slight decreasing nickel content with increasing weld depth can be observed. The upper and the middle regions contain approximately 8.5–9.0 wt.% nickel. On contrary, the nickel content occasionally drops below 8 wt.% in the bottom region. This decreasing trend is only partially reflected in the microstructural results as shown in Fig. 10.

Figure 14 shows the nickel content along the weld depths when welding with weld pool backing. Comparing the results with those presented in Fig. 13, no significant

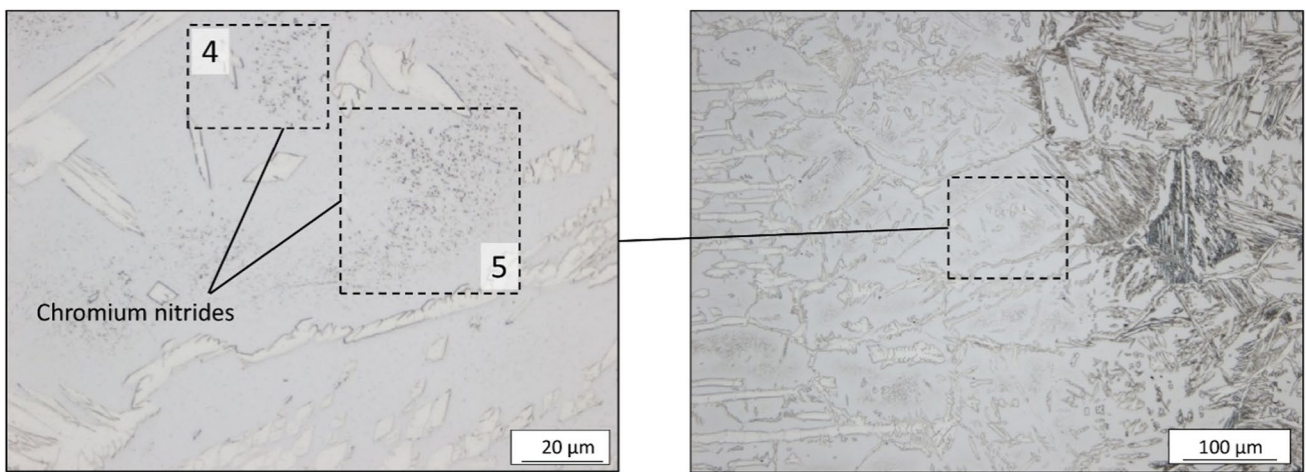


Fig. 12 Finely dispersed chromium nitrides in the HAZ revealed after electrochemical etching with oxalic acid (test 2; pos. A)

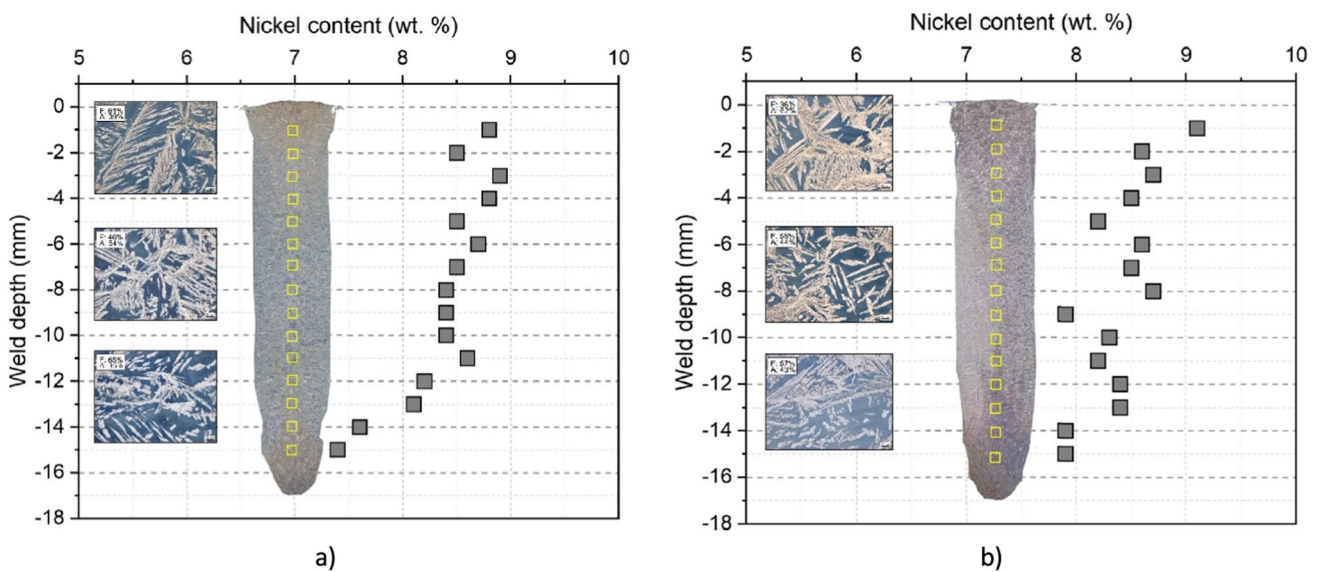


Fig. 13 Distribution of the nickel content over the weld depth for test 1 (a pos. A; b pos. B)

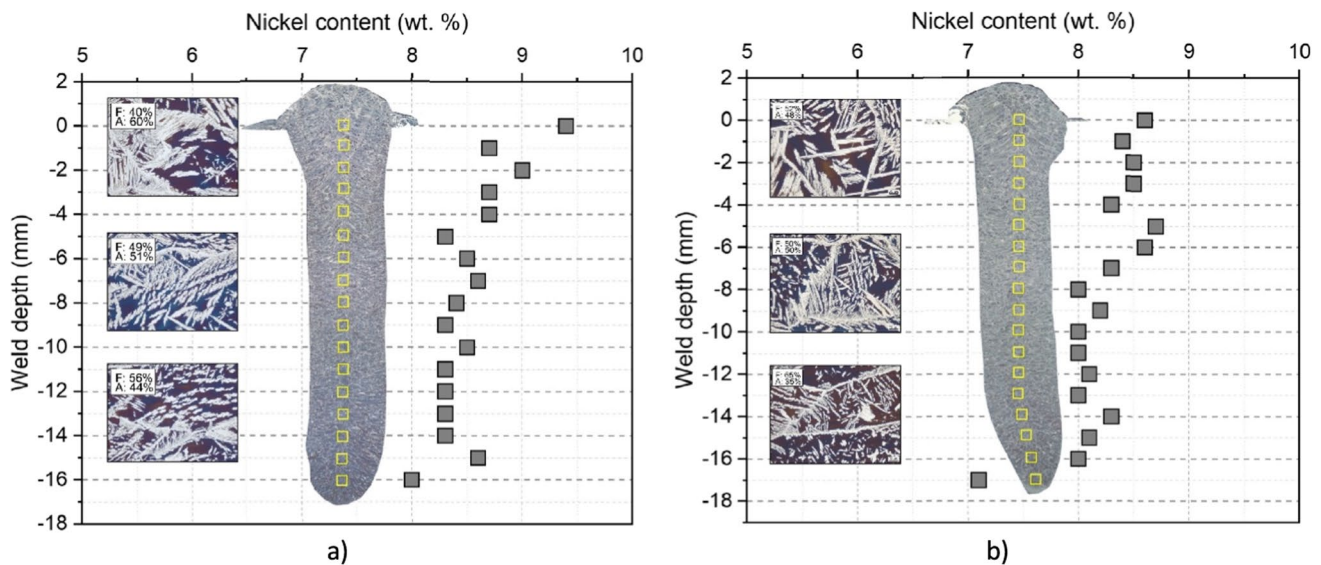


Fig. 14 Distribution of the nickel content over the weld depth for test 2 (a pos. A; b pos. B)

Table 4 The values obtained from the CGHE

Specimen	Test 1		Test 2		Base metal -
	Top	Bottom	Top	Bottom	
Nitrogen content (wt. %)	0.1324	0.1316	0.1337	0.1382	0.183*

*Obtained by OES

difference can be observed. In pos. A., the top region has a higher nickel content than that of pos. B or of the two specimens extracted from the test 1. This leads to higher austenite fractions as can be seen in Fig. 10.

3.3 Nitrogen loss

A further aspect was the nitrogen loss in the fusion zone. The obtained nitrogen content values are summarized in Table 4. Compared to the base metal, an absolute loss of approximately 0.05 wt.% occurred during welding. This results in a relative loss of 25–30%. By analyzing the individual values, no significant difference either between the test runs or between the individual regions of the weld metal are shown.

3.4 Mechanical properties

Further examinations focused on the mechanical properties of the produced joints. Figure 15a presents a boxplot to display the hardness values in the different regions of the FZ. Here, the values measured in the same test plate and the same FZ region were summarized. Hence, one box

represents two rows of measurements in the respective FZ region (bottom, middle, or top), one in the pos. A, and a second one in the pos. B. The boxes show the median values, as well as the first and third quartiles. The whiskers represent a distance of 1.5 times the interquartile range (IQR). Analyzing the acquired values in the case of test 1, it can be stated that there is no significant difference in the mean values between the three regions of the FZ. However, the lower regions possess a larger deviation in terms of their hardness values. Generally, all values are in the range between approximately 250 and 280 HV. In exceptional cases, the hardness value drops below 250 HV, which is comparable to that of the base metal. Taking test 2 into account, a different phenomenon occurs. The hardness values in the lower regions are consistently higher than those in the top and the middle regions and are located in the range of 270–290 HV. The hardness values in the middle region, as well as in the top region, are comparable to those obtained in the test 1. Figure 15b depicts a hardness distribution measured normal to the weld centerline in the case of test 2 pos. B. To summarize, the measured hardness values in the FZ are higher than those in the BM, not only in the bottom region, but in all regions of all plates. However, the maximal allowed average hardness (310 HV) defined by the API TR 938-C [38] was not exceeded.

Figure 16a presents the acquired impact energy values of the different samples and FZ regions. The rectangular bars show the mean values, while the error bars represent the minimum and the maximum values. As can be seen, the impact energy values are between 270 and 310 J, fulfilling the requirements formulated by various standards. According to the NORSOK M-601 [34], the minimum average

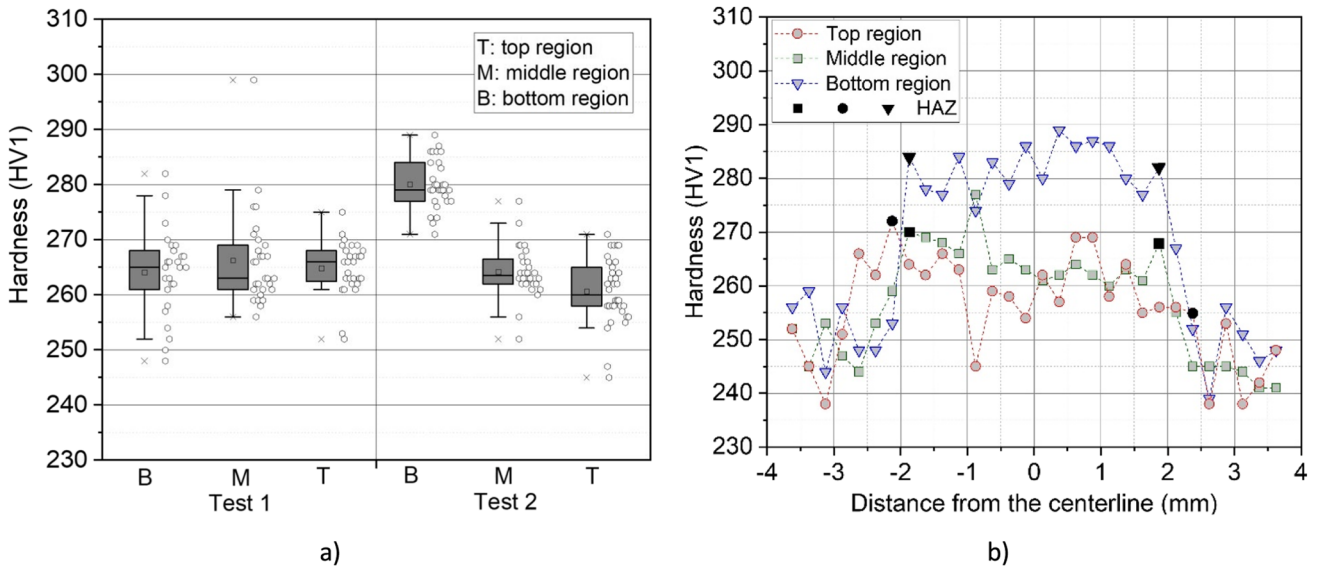


Fig. 15 Boxplots of the hardness values in the different regions of the FZ (a) and a hardness distribution measured on test 2 (pos. B) (b)

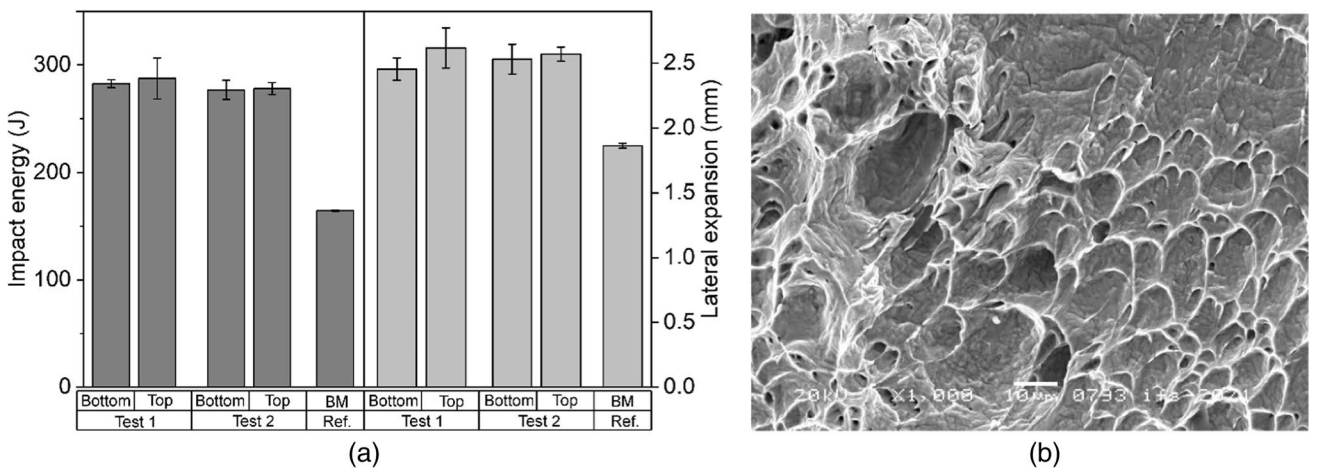


Fig. 16 The obtained impact energy values (a) and a SEM image from the fracture surface (b) captured on the Charpy-V specimen extracted from the test 1

absorbed energy shall amount to at least 27 J at -46°C . EN ISO 17781 [37] requires a minimum mean absorbed energy of 50 J at -46°C with a supplementary requirement of having no individual values under 40 J. By analyzing the obtained values, only a small difference can be detected between the top region and the bottom region. The specimens extracted from the top region have a slightly higher average absorbed impact energy and also a greater lateral expansion than those from the bottom region. In terms of weld pool backing, no significant difference was detected, neither in the impact energy values nor regarding the lateral expansion. Figure 16b shows an image from the fracture surface captured by SEM. The morphology points out the

ductile behavior of the structure, which also confirms the statement formulated during analyzing the absorbed impact energies. Furthermore, the nickel content was measured by analyzing the EDS spectrum obtained on the fracture surfaces. The acquired nickel content values are between 7.4 and 7.7 wt.%. Considering the results of the EDS measurements along the weld centerline (see Fig. 13) and the usual error in calculating the chemical composition by means of this procedure, it can be stated that the crack propagated through the weld metal without fracture path deviation (FPD). The obtained values are also greater than that of the base metal (BM), which also confirms the non-occurrence of the FPD.

Table 5 The values obtained at the tensile tests

Specimen	R_m (MPa)	$R_{p0.2}$ (MPa)	A (%)	Fracture location
Test 1 (top/bottom)	751/748	551 / 547	40.9*/41.8*	BM/BM
Test 2 (top/bottom)	744/744	533 / 539	39.0*/40.1*	BM/BM
Base material requirements	640–840	≥ 460 MPa	> 25.0	-

*Total engineering strain on the reduced section

**Fig. 17** A tensile specimen, extracted from the test 2—bottom region, after fracture

Table 5 shows the results obtained in the tensile testing. The fracture occurred in the base material in all cases. Figure 17 illustrates a specimen from test 2 after fracture.

4 Discussion

The goal of this study was to apply a nickel-based filler wire for providing a stronger austenite formation, which is generally suppressed by rapid cooling and nitrogen effusion. To ensure a sufficient dilution between the filler wire and the base material, a multi-beam technique with integrated beam oscillation was applied. The EDS measurements along the weld centerline showed a good dilution in both cases (tests 1 and 2), especially when considering the weld width/depth ratio. Even the lowest regions of the FZ can be adequately enriched with nickel, leading to a nickel content above 8 wt.%. Welding without weld pool backing, hence using an open keyhole, does not lead to a further improvement of the dilution. A small difference of 1–1.5 wt.% Ni remains after solidification. This slightly inhomogeneous distribution is also reflected in the austenite fractions, particularly when welding with weld pool backing despite the nearly unaltered nickel distribution compared to the weldment produced without weld pool backing. This may be attributed to the different thermal conditions resulting from the difference between the keyhole modes. In summary, it can be stated that, depending on the present chemical composition, nickel content of 8–9 wt.% leads to a balanced microstructure containing 40–60% ferrite under the cooling conditions, which are usual for power beam processes. Considering the common specifications that the ferrite fraction should be in the range of 35–65%, weldments with such a microstructure may gain industrial relevance if other requirements related to mechanical and corrosion properties are also met. The balanced microstructure moreover impedes the formation of chromium nitrides, since the nitrogen can be sufficiently

solved in the austenitic phase. Chromium nitride appears solely in the HAZ, as its chemical composition cannot be influenced by additional material. The concentrated heat input inevitably led to the formation of large ferrite grains, in which chromium nitride precipitates. This was adequately detected by using electrochemical etching.

As a result of the balanced microstructure, the fusion zone is characterized by a high toughness. The measured values are between 270 and 310 J, which are higher by a factor of 5 than that required by the standards [34, 37]. The ductile behavior is further pointed out by observing the fracture morphology captured by SEM. The top regions consequently had slightly higher absorbed energy values and greater lateral expansions, which correlates with the higher average austenite fractions measured there. However, this difference is marginal. By comparing the obtained hardness values within the sample, no significant difference can be seen when welding without weld pool backing. Yet the distribution of the austenite was also very homogeneous. A different phenomenon appears when welding with weld pool backing. The inhomogeneous distribution of the austenite is more clearly reflected in the hardness values. The bottom region of the FZ has consistently higher hardness values than the top and middle regions. These values are also higher than those obtained in the bottom regions of the plate welded without weld pool backing (test 1), despite the ferrite fractions are nearly equal. In terms of the nickel content, a small difference can be seen; test 2 has consistently a higher nickel content (difference: 0.3–0.4 wt.%) in the root region than test 1. The nitrogen losses in test 1 do not exceed the losses in test 2. The influence of the backing bar, serving also as a heat sink, can therefore be taken into consideration to be a possible reason for the difference in the hardness values, as experienced in other studies [40]. A further observation is that the top region of test 2 (welded with weld pool backing) had the lowest median and mean hardness, which correlates with the low amount of ferrite (especially at pos. A), detected in that region, as shown in Fig. 10.

Based on the obtained results, further aspects emerged. Remelting the cap with TIG or a simultaneous EBW would greatly reduce the costs, as the expenses of machining could be minimized or even eliminated. Whether this step increases or decreases the ferrite content should be thoroughly investigated. Due to the relatively high nickel content, stress corrosion cracking may be of concern and can also be the subject of further experiments. Moreover, EDS mapping would also be of interest to describe the distribution of the alloying elements not only along the centerline but also in the entire FZ.

5 Conclusions

In this study, 2205 DSS plates were welded with EB using a multi-beam technique and a nickel-based filler wire. Based upon the findings, the following conclusion can be drawn:

- Using the multi-beam technique and an “infinity”-shaped oscillation pattern, a very good dilution between the filler wire and the base material was achieved. The upper regions of the FZ contain approximately 9 wt.% nickel, while the lower regions exhibit a nickel content of roughly 8 wt.%.
- In terms of dilution, there is no difference between welding with an open keyhole (welding without weld pool backing) and that without an open keyhole (welding with weld pool backing). The nickel content along the weld penetration shows the same decreasing trend in both cases.
- Deploying the nickel-based filler wire resulted in a balanced microstructure even in the lower regions of the fusion zone. The lower regions exhibit a slightly higher ferrite fraction than the upper ones. This phenomenon is more pronounced when welding with weld pool backing. This reflects the decreasing trend in the nickel content.
- The HAZ around the weld cap (nail-head) is more pronounced and possesses a width of 200–250 µm. In the lower regions, the HAZ is narrower.
- The hardness values are higher than those of the base metal. The highest values were measured in the root region of the FZ when welding with weld pool backing. These values are in the range of 270–290 HV.
- The impact toughness values are located in the range of 270–310 J, indicating a tough behavior of the weld metal.
- In tensile testing, the fracture occurred in the base metal.

Acknowledgments The authors would like to express their appreciation for the base material provided by Outokumpu Nirosta GmbH and for the filler wire provided by SFG Schweißtechnik Fachhandel Gubelas GmbH.

Author contribution T. Tóth: Conceptualization, formal analysis, investigation, methodology, visualization, writing—original draft

J. Hensel: Conceptualization, data curation, project administration, supervision, validation, writing—review and editing

A-C. Hesse: Project administration, supervision, validation, writing—review and editing

K. Dilger: Funding acquisition, resources, supervision

All authors have read and agreed to the document.

Funding Open Access funding enabled and organized by Projekt DEAL. The IGF-research project 20.622N of the Research Association FOSTA Forschungsvereinigung Stahlanwendung e.V. is funded by the AiF within the program to promote Joint Industrial Research (IGF) by the Federal Ministry for Economic Affairs and Climate Action, following a decision by the German Bundestag.

Data availability The raw/processed data required to reproduce these findings cannot be shared at this time due to time limitations.

Declarations

Conflict of interest The authors declare no conflict of interest.

Open Access This article is licensed under a Creative Commons Attribution 4.0 International License, which permits use, sharing, adaptation, distribution and reproduction in any medium or format, as long as you give appropriate credit to the original author(s) and the source, provide a link to the Creative Commons licence, and indicate if changes were made. The images or other third party material in this article are included in the article's Creative Commons licence, unless indicated otherwise in a credit line to the material. If material is not included in the article's Creative Commons licence and your intended use is not permitted by statutory regulation or exceeds the permitted use, you will need to obtain permission directly from the copyright holder. To view a copy of this licence, visit <http://creativecommons.org/licenses/by/4.0/>.

References

1. Lippold JC, Kotecki Damian J (2005) Welding metallurgy and weldability of stainless steels. John Wiley & Sons, Hoboken, New Jersey, pp 230–234
2. Gunn R N (1997) Duplex stainless steels: microstructure, properties and applications. Abington Publishing, pp 1–2
3. Westin E (2010) Microstructure and properties of welds in the lean duplex stainless steel LDX 2101. Licentiate Thesis, Royal Institute of Technology, Sweden, pp 3–5
4. AWS Welding Handbook 2: Welding Processes. Eight Edition (1997), pp 671–712
5. Pickle T, Henry N, Morriss P, Tennis L, Wagner D, Baumer R (2019) Root pass microstructure in super duplex stainless steel multipass welds. *Welding Journal* 98:123. <https://doi.org/10.29391/2019.98.010>
6. Ku JS, Ho NJ, Tjong SC (1997) Properties of electron beam welded SAF 2205 duplex stainless steel. *J Mater Process Technol* 63(1):770–775. [https://doi.org/10.1016/S0924-0136\(96\)02721-5](https://doi.org/10.1016/S0924-0136(96)02721-5)
7. Knyazeva M, Pohl M (2013) Duplex steels: Part I: GENESIS, Formation, Structure. *Metallography, Microstructure, and Analysis* 2(2):113–121. <https://doi.org/10.1007/s13632-013-0066-8>
8. Tóth T, Krasnorutskyi S, Hensel J, Dilger K (2021) Electron beam welding of 2205 duplex stainless steel using pre-placed

- nickel-based filler material. *Int J Press Vessels Pip* 191:104354. <https://doi.org/10.1016/j.ijpvp.2021.104354>
9. Lippold JC, Baeslack WA, Varol I (1992) Heat-affected zone liquation cracking in austenitic and duplex stainless steels. *Welding J Welding Res Suppl* 1(1):1–14 (http://files.aws.org/wj/supplement/WJ_1992_01_s1.pdf)
 10. Hertzman S, Ferreira PJ, Brolund B (1997) An experimental and theoretical study of heat-affected zone austenite reformation in three duplex stainless steels. *Metall Mater Trans* 28A:277–285. <https://doi.org/10.1007/s11661-997-0130-6>
 11. Corolleur A, Fanica A, Passot G (2015) Ferrite content in the heat affected zone of duplex stainless steels. *BHM* 160(9):413–418
 12. Varbai B, Pickle T, Májlinger K (2019) Effect of heat input and role of nitrogen on the phase evolution of 2205 duplex stainless steel weldment. *Int J Press Vessels Pip* 176:103952. <https://doi.org/10.1016/j.ijpvp.2019.103952>
 13. Yang Y, Yan B, Li J, Wang J (2011) The effect of large heat input on the microstructure and corrosion behaviour of simulated heat affected zone in 2205 duplex stainless steel. *Corros Sci* 53:3756–3763. <https://doi.org/10.1016/j.corsci.2011.07.022>
 14. Hosseini VA, Karlsson L (2019) Physical and kinetic simulation of nitrogen loss in high temperature heat affected zone of duplex stainless steels. *Materialia* 6:100325. <https://doi.org/10.1016/j.mtla.2019.100325>
 15. Hosseini VA, Wessman S, Hurtig K, Karlsson L (2016) Nitrogen loss and effects on microstructure in multipass TIG welding of a super duplex stainless steel. *Mater Des* 98:88–97. <https://doi.org/10.1016/j.matdes.2016.03.011>
 16. Krasnorutskiy S, Keil D, Schmigalla S, Zinke M, Heyn A, Pries H (2012) Metallurgical investigations on electron beam welded duplex stainless steels. *Welding in the World* 56:34–40. <https://doi.org/10.1007/BF03321393>
 17. Krasnorutskiy S, Kipp C, Hensel J, Kaestner P, Hartwig S, Bräuer G, Dilger K (2018) Metallurgical investigation of electron beam welded duplex stainless steel X2CrNiMoN22-5-3 with plasma nitrided weld edge surfaces. *Mater Test* 60:577–582. <https://doi.org/10.3139/120.111190>
 18. Schmigalla S, Krasnorutskiy S, Zinke M, Heyn A (2014) Corrosion behavior of electron beam welded duplex stainless steels. *Mater Corros* 66(5):442–452
 19. Keskitalo M, Mäntyjärvi K, Sundqvist J, Powell J, Kaplan AFH (2015) Laser welding of duplex stainless steel with nitrogen as shielding gas. *J Mater Process Technol* 216:381–384. <https://doi.org/10.1016/j.jmatprotec.2014.10.004>
 20. Lai R, Cai Y, Wu Y, Li F, Hua X (2016) Influence of absorbed nitrogen on microstructure and corrosion resistance of 2205 duplex stainless steel joint processed by fiber laser welding. *J Mater Process Technol* 231:397–405. <https://doi.org/10.1016/j.jmatprotec.2016.01.016>
 21. Pamuk S, Sojiphan K (2018) Effects of argon-nitrogen backing gas ratios on microstructure and corrosion resistance of duplex stainless steel pipe ASTM A790 welds by gas tungsten arc welding process. *Materials Today: Proceedings*, vol. 5, 3. Part 2:9512–9518. <https://doi.org/10.1016/j.matpr.2017.10.132>
 22. Reyes-Hernández D, Manzano-Ramírez A, Encinas A, Sánchez-Cabrera VM, Jesús ÁM, García-García R (2017) Addition of nitrogen to GTAW welding duplex steel 2205 and its effect on fatigue strength and corrosion. *Fuel* 198:165–169. <https://doi.org/10.1016/j.fuel.2017.01.008>
 23. Zhang Z, Jing H, Xu L, Han Y, Zhao L, Zhou C (2017) Effects of nitrogen in shielding gas on microstructure evolution and localized corrosion behavior of duplex stainless steel welding joint. *Appl Surf Sci* 404:110–128. <https://doi.org/10.1016/j.apsusc.2017.01.252>
 24. Fey A, Ulrich S, Jahn S, Schaaf P (2020) Numerical analysis of temperature distribution during laser deep welding of duplex stainless steel using a two-beam method. *Welding in the World* 64:623–632. <https://doi.org/10.1007/s40194-020-00857-8>
 25. Krasnorutskiy S, Pries H, Zinke M, Keil D (2013) Metallurgical influence of multi-beam technology on duplex stainless steel welds. *Welding in the World* 57:487–494. <https://doi.org/10.1007/s40194-013-0042-6>
 26. Maurya AK, Pandey C, Chhibber R (2021) Dissimilar welding of duplex stainless steel with Ni alloys: a review. *Int J Press Vessels Pip* 192:104439. <https://doi.org/10.1016/j.ijpvp.2021.104439>
 27. Wu HC, Tsay LW, Chen C (2004) Laser beam welding of 2205 duplex stainless steel with metal powder additions. *ISIJ Int* 44(10):1720–1726
 28. Strasse A, Gumenyuk A, Rethmeier M (2019) Quality improvement of laser welds on thick duplex plates by laser clad buttering. Munich, Germany
 29. Tóth T, Hensel J, Dilger K (2021) Effect of beam oscillation parameters on the weld geometry and dilution in electron beam welding of duplex stainless steels with nickel-based filler wire. *Proceedings of the 6th International Electron Beam Welding Conference*, pp 27–33
 30. Rührich K, Mangler M (2012) Elektronenstrahl-Mehrprozessentechnik – Schweißen mit integrierter Wärmebehandlung (in German). *HTM Journal of Heat Treatment and Materials* 67(1):22–30. <https://doi.org/10.3139/105.110129>
 31. Hammar O. S. U (1979) Influence of steel composition on segregation and microstructure during solidification of austenitic stainless steels. *Solidification and casting of metals*, Conference
 32. ASTM E562 – 11. Standard test method for determining volume fraction by systematic manual point count, pp 1–5
 33. ASTM E1245-03. Standard practice for determining the inclusion or second-phase constituent content of metals by automatic image analysis, pp 1–7
 34. NORSOK M-601 (2016) Welding and inspection of piping, p 13
 35. NORSOK M-630 (2004) Material data sheets for piping, pp 21–22
 36. EN ISO 148-1:2017-5. Metallic materials - Charpy pendulum impact test - Part 1: test method, pp 8–16
 37. EN ISO 17781 (2017-08). Petroleum, petrochemical and natural gas industries - test methods for quality control of microstructure of ferritic/austenitic (duplex) stainless steels, p 12
 38. American Petroleum Institute. Technical Report 938-C. (2011) Use of duplex stainless steels in the oil refining industry, p 39
 39. Westin EM, Fellman A (2010) Effect of laser and laser hybrid welding on the corrosion performance of a lean duplex stainless steel. *J Laser Appl* 22(4):150–158. <https://doi.org/10.2351/1.3533146>
 40. Babu PD, Gouthaman P, Marimuthu P (2019) Effect of heat sink and cooling mediums on ferrite austenite ratio and distortion in laser welding of duplex stainless steel 2205. *Chinese J Mechanical Eng* 32:50. <https://doi.org/10.1186/s10033-019-0363-5>

Publisher's note Springer Nature remains neutral with regard to jurisdictional claims in published maps and institutional affiliations.